FULL PAPER

NANO · MICRO
small
www.small-journal.com
Check for updates

Bottom-Up Assembly of Functional Intracellular Synthetic Organelles by Droplet-Based Microfluidics

Oskar Staufer,* Martin Schröter, Ilia Platzman,* and Joachim P. Spatz*

Bottom-up synthetic biology has directed most efforts toward the construction of artificial compartmentalized systems that recreate living cell functions in their mechanical, morphological, or metabolic characteristics. However, bottom-up synthetic biology also offers great potential to study subcellular structures like organelles. Because of their intricate and complex structure, these key elements of eukaryotic life forms remain poorly understood. Here, the controlled assembly of lipid enclosed, organelle-like architectures is explored by droplet-based microfluidics. Three types of giant unilamellar vesicles (GUVs)-based synthetic organelles (SOs) functioning within natural living cells are procedured: (A) synthetic peroxisomes supporting cellular stress-management, mimicking an organelle innate to the host cell by using analogous enzymatic modules; (B) synthetic endoplasmic reticulum (ER) as intracellular light-responsive calcium stores involved in intercellular calcium signalling, mimicking an organelle innate to the host cell but utilizing a fundamentally different mechanism; and (C) synthetic magnetosomes providing eukaryotic cells with a magnetotactic sense, mimicking an organelle that is not natural to the host cell but transplanting its functionality from other branches of the phylogenetic tree. Microfluidic assembly of functional SOs paves the way for high-throughput generation of versatile intracellular structures implantable into living cells. This in-droplet SO design may support or expand cellular functionalities in translational nanomedicine.

1. Introduction

The employment of droplet-based microfluidics for the controlled assembly of artificial cell-like structures has revolutionized the field of bottom-up synthetic biology.[1] These water-in-oil (w/o) droplet compartments provide a cell-like discrimination between intra- and extracellular space. Within such synthetic cells, complex molecular machineries like tubulin spindles and coupled transcription-translation systems have been brought to life.[2,3] Moreover, adding microfluidic double-emulsion techniques and charge-mediated formation of cell-sized giant unilamellar vesicles (GUVs) inside such droplets has even allowed the production of lipid enclosed structures that mimic complex cellular behaviours like adhesion and migration.[4,5]

Apart from the assembly of synthetic cells, the field of bottom-up synthetic biology has also focused on the controlled assembly of sub-cellular structures like organelles. Organelles are considered a hallmark of eukaryotic life forms and provide a confined intracellular reaction space with an intriguing structure-function relation. Although phase-separated, membraneless organelles have recently been described, most eukaryotic organelles are surrounded by one lipid bilayer (e.g., the endoplasmic reticulum (ER), endosome or Golgi apparatus) or even two lipid bilayers (e.g., nucleus, mitochondria, or chloroplasts). Rebuilding such lipid enclosed reaction spaces has turned into a fundamental ambition of synthetic biology. The goal is to not only explore their working principles but to also develop cellular implants able to rescue cells with dysfunctional organelles.[6] One example is the design of peroxisome-like polymerosomes with entrapped horseradish peroxidase enzymes that are able to support cellular redox homeostasis.[7] Further examples include photosystems from plants and bacteria that have been reconstituted into lipid vesicles in vitro, thereby recreating chloroplasts with their ability to produce ATP by harvesting light energy.[8] In addition, membraneless synthetic organelles (SOs) have also been implanted into cells to perform orthogonal translation, resulting in an expansion of the canonical set of amino acids.[9]

In studies aimed at exploring the function of membrane-enclosed organelles using their synthetic doppelgangers, the respective SO production pipeline ideally comprises a high

O. Staufer, M. Schröter, Dr. I. Platzman, Prof. J. P. Spatz
Department for Cellular Biophysics
Max Planck Institute for Medical Research
Jahnstraße 29, 69120 Heidelberg, Germany
E-mail: Oskar.Staufer@mr.mpg.de; Ilia.platzman@mr.mpg.de;
Joachim.Spatz@mr.mpg.de
O. Staufer, M. Schröter, Dr. I. Platzman, Prof. J. P. Spatz
Institute for Physical Chemistry
Department for Biophysical Chemistry
University of Heidelberg
Im Neuenheimer Feld 253, 69120 Heidelberg, Germany
O. Staufer, Dr. I. Platzman, Prof. J. P. Spatz
Max Planck-Bristol Centre for Minimal Biology
University of Bristol
1 Tankard's Close, Bristol BS8 1TD, UK
Prof. J. P. Spatz
Max Planck School Matter to Life
Jahnstraße 29, D-69120 Heidelberg, Germany

control over individual SO elements. In this way, single properties like the protein load, membrane composition, or size can be varied and their function individually assessed. Moreover, when attempting to implant SOs for therapeutic procedures, a substantially high and cost-efficient production throughput is essential. Toward this end, droplet-based microfluidic technology is a promising approach for easily controllable, high-throughput GUV assembly.[4] Previous reports also highlight that microfluidic droplets and therefore GUVs produced by in-droplet formation can be precisely tuned in their composition and physical characteristics (e.g., charge).[10–12] These vesicles are especially suited to act as SOs, as their lipid shell closely resembles the membrane of natural organelles. Moreover, passive endocytotic uptake into the intracellular space and the cytotoxicity of organelle-sized lipid vesicles have both been studied extensively for many decades in several cell types as well as in vivo.[13] Moreover, studying the uptake and integration of lipid-enclosed structures into cells is of especially high interest as it may shed light on the origin of eukaryotic life forms as explained by the theory of endosymbiosis. Here, the stable integration of SOs as well as the functional fusion of their molecular machinery with the host cell's inner life could provide new insights into the prehistoric formation of organelles.

We here explore high-throughput microfluidic production of GUVs for the assembly of lipid-enclosed synthetic organelles and investigate their functionality within living cells. We focus on three concepts: (1) the assembly of SOs that mimic the function of a host cell's organelle using its naturally given repertoire of enzymes, (2) the assembly of SOs that exert a function intrinsic to the host cell utilizing an alternate design principle that is based on a different structure–function relationship, and (3) the assembly of SOs that equip the host cell with an entirely new, nonintrinsic functionality.

2. Results

2.1. Mimicking the Natural Functionality of Organelles

For the assembly of the first set of SOs, we produced GUVs using previously reported techniques for in-droplet GUV formation.[4,10,11] In brief, w/o droplets are produced using a fluorinated oil phase containing a droplet-stabilizing polyethylene glycol–perfluoropolyether (PEG-PFPE) surfactant at a polydimethylsiloxane-based (PDMS) microfluidic flow focusing T-junction. The oil phase is additionally supplemented with PFPE carboxylic acid, which upon droplet formation introduces a negative charge at the water droplet periphery (**Figure 1**a). The water phase contains negatively charged small unilamellar vesicles (SUVs) with a desired lipid composition as well as a millimolar concentration of $MgCl_2$. The Mg^{2+} cations mediate the formation of a supported lipid bilayer by fusion of the SUVs on the inner droplet polymer shell, eventually producing a droplet-stabilized GUV (dsGUV).[10] Hereby, the Mg^{2+} ions mediate the interaction between the negatively charged droplet periphery and the negatively charged SUVs. This process can also be performed with other divalent cations like Ca^{2+}. This charge-mediated assembly allows for the encapsulation of biomolecular content like proteins or nucleic acids and other inorganic particles suspended in the aqueous SUV solution used for droplet production.[11] The microfluidic technology not only provides a well-controlled production pipeline but also a means for high-throughput assembly of such mechanically stabilized GUVs. By adding a low molecular weight perfluoro-octanol (PFO) destabilizing surfactant to the collected dsGUVs, the w/o emulsification can be broken and the formed GUVs are released into an aqueous environment (e.g., cell culture medium), allowing for their incubation with living cells in vitro (Figure 1b).
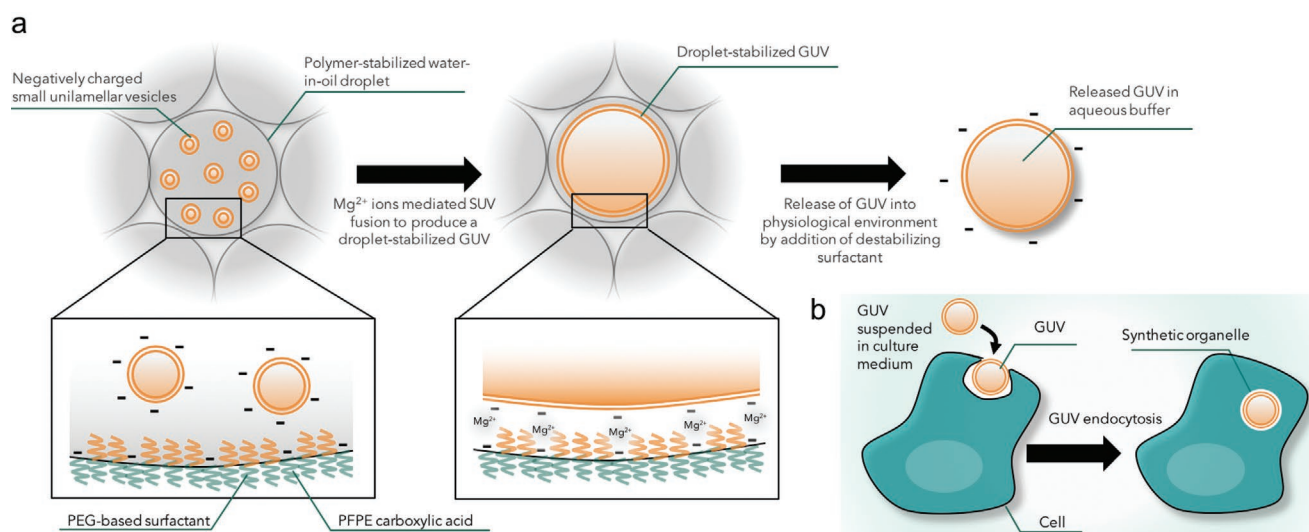
Figure 1. Schematic representation of the GUV formation process inside water-in-oil droplets and GUV uptake. a) Polymer-stabilized water-in-oil droplets are produced containing negatively charge small unilamellar vesicles. The droplets are stabilized by a PFPE-PEG surfactant and PFPE carboxylic acid, which introduces a negative charge to the droplet periphery. Mg^{2+} ions mediate the attachment of the negatively charged SUVs to the droplet periphery and subsequently the fusion of SUVs to create as supported lipid bilayer. When the whole droplet periphery is cover with such a bilayer, this produces a droplet-stabilized GUV which can subsequently be released from its oil-polymer shell into an aqueous phase by addition of a demulsifier (e.g., destabilizing surfactant). b) For integration of GUVs as SOs elements into eukaryotic cells, GUVs are added to the culture medium. The GUVs are passively uptaken by endocytic mechanisms, forming an SOs inside the cell plasma.
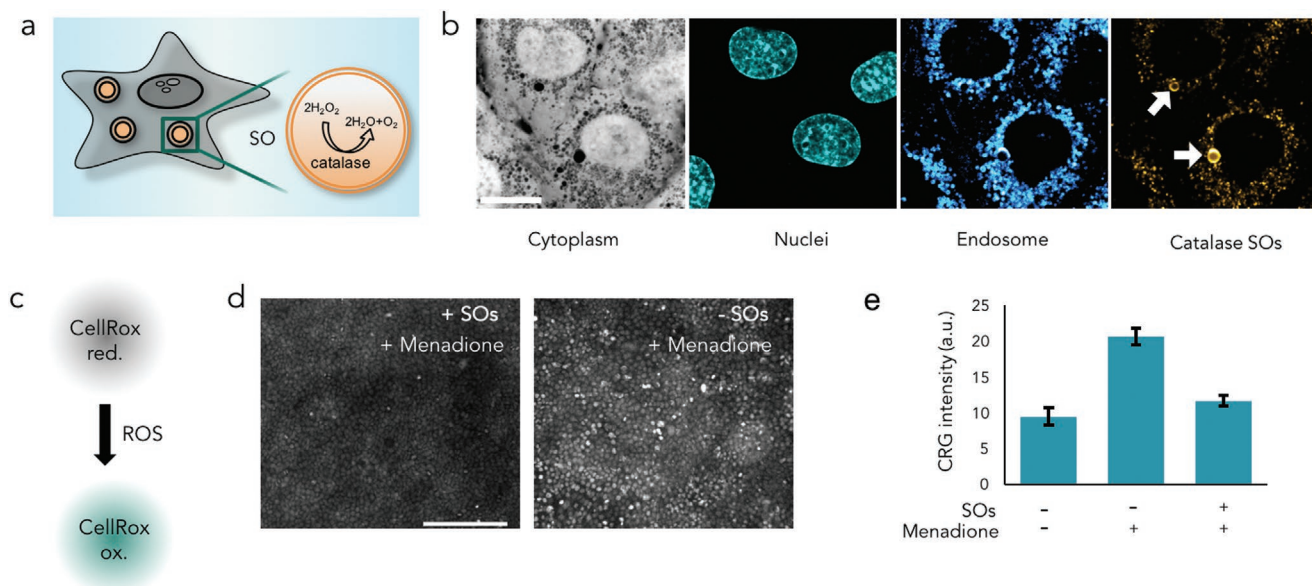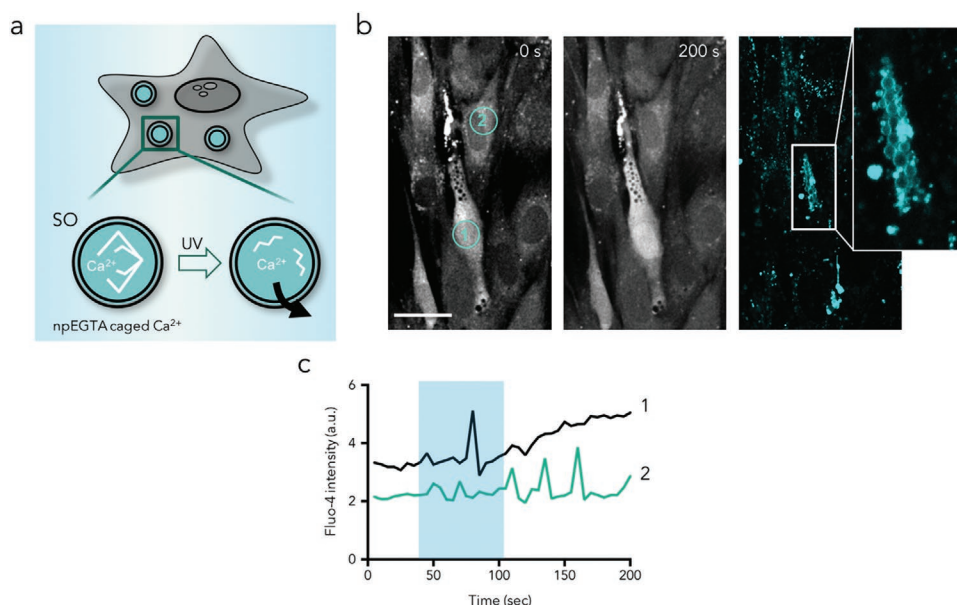
Figure 2. Mimicking the natural functionality of organelles by peroxisome-like SOs. a) Schematic representation of a peroxisome-like SO-loaded cell. The peroxisome-like SO consists of an internalized, bovine catalase-harbouring GUV able to catalyse the breakdown of hydrogen peroxide. b) Representative fluorescence confocal microscopy images of HaCaT cells incubated with peroxisome-like SOs. The cytoplasm was stained with CellTracker Green (grey), nuclei were stained with Hoechst 33 342 (cyan), endosomes were stained with wheat germ agglutinin Alexa647-conjugate (blue), and SOs (white arrows) contained rhodamine B-conjugated lipids for visualization (yellow). The scale bar is 15 µm. c) Schematic representation of CRG staining based on the ROS-mediated oxidation of the weakly fluorescent molecule resulting in a bright fluorophore for intracellular ROS quantification. d) Epifluorescence microscopy images of HaCaT epithelial monolayers treated for 1 h with 25×10^{-6} M menadione and stained with CRG for 20 min. Cell monolayers were either loaded with peroxisome-mimicking SOs (+SOs left image) or left without SOs (-SOs right image). Cells without SOs show stronger CRG staining, indicating higher ROS levels. e) Quantitative plate-reader based assessment of the CRG staining intensity in HaCaT monolayers. Cells were either treated with 25×10^{-6} M menadione for 1 h or left untreated. Cells harbouring peroxisome-like SOs containing 2.7×10^{-6} M bovine catalase show ROS levels comparable to those of unstressed cells. Mean ± SD from three technical replicates are shown.

Our first approach was aimed at producing peroxisome-mimicking SOs by incorporating catalase enzymes into the GUV lumen. Peroxisomes are key regulators of cellular redox homeostasis and rely on catalase-mediated hydrogen peroxide breakdown for their functionality (**Figure 2**a). Although different organelles comprise different lipid compositions, all of them have a negative net-charge and phosphatidylcholin is the most abundant lipid.[14] In order to mimic this membrane composition, we produced GUVs composed of 20 mol% EggPG, 79 mol% EggPC, and 1 mol% rhodamine B-conjugated lipids (for imaging) containing micromolar amounts of bovine catalase. After 24 h in vitro incubation with immortalized human HaCaT keratinocytes we used fluorescence confocal microscopy to observe the formation of an encircling endosomal membrane due to intracellular uptake of the respective GUVs by endocytic mechanisms (Figure 2b). Keratinocytes were chosen, because many inflammatory diseases of the skin as well as carcinoma progression and deregulated wound healing have been closely linked to deregulated redox homeostasis and oxidative stress.[15] Importantly, we did not observe cytotoxic effects of GUV incubation with cells, even for extended observation periods of 72 h (Figure S1, Supporting Information). In order to assess whether our synthetic peroxisomes are able to reduce oxidative stress and support the cellular antioxidative machinery of epithelial monolayers, we measured intracellular levels of reactive oxygen species (ROS) by CellRox Green (CRG) staining (Figure 2c). CRG is a weakly fluorescent, cell-permeable dye that upon oxidation by ROS emits a bright green fluorescence,

thereby allowing for quantification of intracellular ROS levels. We treated the cells layers with an extrinsic oxidative stressor menadione (25×10^{-6} M), which induces a substantial rise in ROS levels.[16] Menadione-stressed epithelial monolayers, loaded with synthetic peroxisomes for 24 h and stained with CRG, showed reduced CRG staining compared to cell layers without synthetic peroxisomes under the fluorescence microscope (Figure 2d). Importantly, before addition of menadione and CRG staining, cell layers were washed twice to exclude any H_2O_2 scavenging by extracellular peroxidases in non-uptaken GUVs. A quantitative analysis revealed that GUVs containing catalase concentrations of as little as 2.7×10^{-6} M could reduce ROS levels down to nearly those of nonstress cultures (Figure 2e). This proves that the implanted catalase-loaded GUVs successfully functioned as peroxisome-like SOs supporting cellular redox-homeostasis under oxidative stress conditions. In the far future, implanting SOs that can mimic and rescue deregulated peroxisome function could provide a novel therapeutic option in this direction.

2.2. Mimicking the Natural Functionality of Organelles Utilizing Synthetic Mechanisms

When aiming to construct SOs that imitate an intrinsic cell function utilizing an alternative synthetic operating principle, we focused on the calcium buffer capacities of the ER and mitochondria. These organelles act as potent calcium storage

Figure 3. Mimicking the natural functionality of organelles utilizing synthetic mechanisms. a) Schematic representation of cells harbouring ER-like and mitochondria-like SOs containing UV-sensitive npEGTA-chelated Ca^{2+} ions. Upon UV irradiation, Ca^{2+} is released from the synthetic SO stores. b) Time-lapse fluorescence confocal microscopy images of a BJ fibroblast monolayer stained with the calcium sensitive dye fluo-4 (grey) and loaded with SOs (cyan) before (left image) and after (middle image) Ca^{2+} release from the SOs (note the increased intensity in cell 1). The scale bar is 30 µm. The region in the magnified inset was illuminated with a 405 nm laser line of the laser-scanning microscope. c) Time course intensity profile of cytoplasmic fluo-4 signal from cells in (b). SOs in cell 1 (pacemaker cell) were illuminated with 405 nm light (the illumination time window is denoted by a turquoise background), thus triggering successive Ca^{2+} increase and firing of calcium action potentials in cell 2 (follower cell).

organelles that regulate calcium homeostasis and release Ca^{2+} for intra- and intercellular signalling. Calcium signalling in fibroblast communication has been studied extensively, because dysfunctional fibroblast electrophysiology is considered to be a major contributor to cardiac fibrosis and deregulated wound healing.[17,18] The sequence of events during fibroblast communication starts with a stimulant inducing pacemaker cell to fire calcium action potentials. The electrophysiological activity of the pacemaker cell then acts as a signal to so-called "follower cells" to increase their intracellular Ca^{2+} levels and also start firing calcium action potentials. The resulting homeostatic, tissue-wide signalling can be visualized with fluorescent calcium sensors (Video S1, Supporting Information) or recorded by electrophysiological measurments.[19,20] The fact that intercellular calcium signalling in fibroblasts builds upon itself to quickly gain momentum and impact, highlights the relevance of calcium buffering systems like the ER and mitochondria for its regulation.

To mimic the function of calcium binding proteins in the ER and mitochondria, we designed synthetic calcium stores by loading the light-sensitive calcium chelator nitrophenyl EGTA (npEGTA) into GUVs composed of 20mol% EggPG, 79mol% EggPC, and 1mol% rhodamine conjugated lipids. The nanomolar affinity of npEGTA for Ca^{2+} increases to $>1 \times 10^{-3}$ M after UV-light exposure and subsequent cleavage of the nitrophenyl group, causing the release of chelated Ca^{2+} ions. In the same way, UV light can be used as an extrinsic stimulus to release free Ca^{2+} from chelators inside GUVs (**Figure 3**a). In order to assess whether the resulting free Ca^{2+} can then diffuse across the GUV membrane, we encapsulated

the respective npEGTA-Ca^2 loaded GUVs together with the fluorescent calcium indicator fluo-4 into w/o droplets (Figure S2, Supporting Information).[11] Upon irradiation of single droplets with a 405 nm laser, we observed fluo-4 intensity successively increase within the GUV and also within the droplet lumen, thus proving successful diffusion of Ca^{2+} across the GUV membrane.

Next, we aimed to implant these calcium-storing GUVs into living fibroblast. Toward this end, we incubated fluo-4-loaded BJ dermal fibroblasts with npEGTA-Ca^{2+}-containing GUVs. Local illumination of the intracellular SOs with a 405 nm laser using a scanning fluorescence confocal microscope showed a prominent transient increase in cytosolic fluo-4 signal intensity (Figure 3b). The signal then spread to unilluminated adjunct follower cells, which subsequently produced calcium action potentials visible as fluo-4 signal intensity spikes (Figure 3c). Altogether, this demonstrates the successful design and implementation of a functional, synthetic, pacemaker-follower cell system based on SOs, which is responsive to extrinsic light stimulation.

## 2.3. Assembly of SOs that Equip the Host Cell with a Noninnate Functionality

Importantly, SOs pave the way toward the implantation of new cellular functionalities that are not innate to a specific cell type. Transplanting synthetic mimics of organelles that are found in one branch of the phylogenetic tree into a cell type of an organism of another branch of the phylogenetic tree could significantly expand the functional repertoire of cellular

**ADVANCED
SCIENCE NEWS**

www.advancedsciencenews.com

NANO · MICRO

small

www.small-journal.com
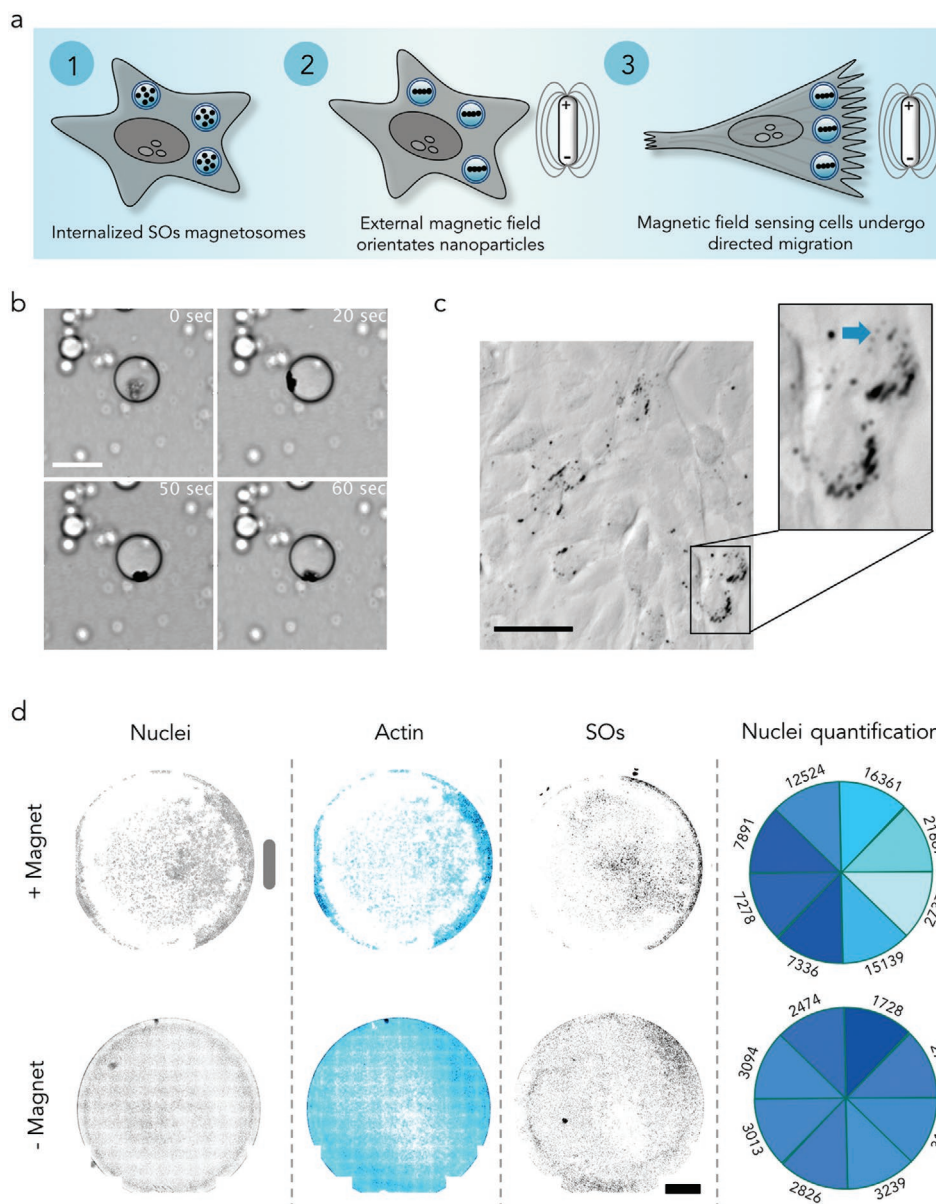
Figure 4. The assembly of SOs that equip the host cell with a completely new, nonintrinsic functionality. a) Schematic representation of synthetic magnetosome-induced polarization and migration in a magnetic field. b) Bright field time-lapse images of Fe_2O_3 nanoparticles incorporated into droplet-stabilized GUVs. During image acquisition, an AlNiCo magnet was placed next to the sample, thus deflecting the nanoparticles. The scale bar is 10 µm. c) Bright field microscopy images of normal rat kidney fibroblasts incubated with magnetosome-like SOs (black dots) and incubated for 48 h next to an AlNiCo magnet. The inset shows the pearl-string-like alignment of SOs (blue arrow) within the cells. The scale bar is 50 µm. d) Epifluorescence microscopy images of normal rat kidney fibroblast cells loaded with magnetosome-like SOs and cultured for 72 h in 15.6 mm diameter wells next to (top row) or without (bottom row) an AlNiCo magnet. Nuclei were stained with Hoechst33342, actin was stained with phalloidin-FITC, and SOs were visualized by rhodamine B incorporation into the lipid membrane. The grey bar indicates the AlNiCo magnet position. The right panel shows the colour-coded results of the automated counting of the nuclei number in the respective regions. The scale bar in the bottom right corner is 3 mm.

machineries in industrial production pipelines or theranostic procedures. For instance, several types of bacteria contain magnetosomes composed of magnetite or greigite that align as pearl-like strings within the cytoplasm and are used for sensing the earth's magnetic field.[21] Such organelles cannot be found in vertebrate cells but could provide novel means for directing cellular polarization and migration (**Figure 4**a). Therefore, for

our third approach, we used microfluidic technology to produce GUVs harbouring Fe_2O_3 nanoparticles ($\approx$50 nm) to function as magnetotactic SOs (see the Experimental Section). When analysing dsGUVs loaded with these ferromagnetic nanoparticles, we observed aggregation as well as sensitive deflection of the aggregates within the GUV lumen by externally applied magnetic fields (Figure 4b).

ADVANCED
SCIENCE NEWS
www.advancedsciencenews.com

NANO · MICRO
small
www.small-journal.com
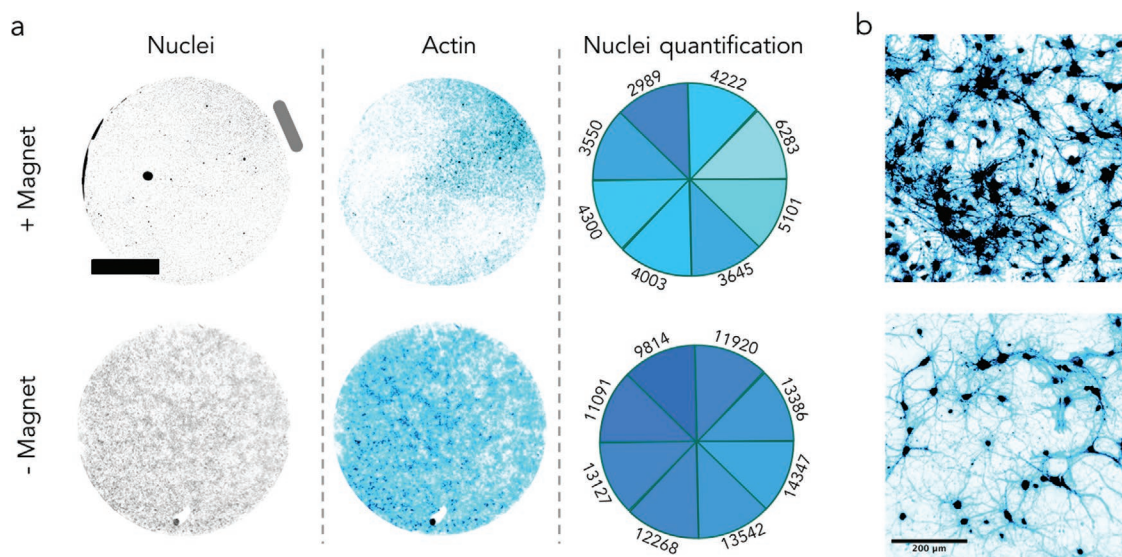
Figure 5. Introduction of magnetosome-like SOs into primary neurons. a) Epifluorescence microscopy images of primary rat hippocampal neurons cultured on 18 mm diameter glass cover slips with magnetosome-like SOs for 96 h next to an AlNiCo magnet (top row) or without a magnet (bottom row). Nuclei were stained with Hoechst33342 and actin was stained with phalloidin-FITC. The grey bar indicates the AlNiCo magnet position. The right panel shows the colour-coded results of the automated counting of the nuclei number in the respective regions. The scale bar in the upper left image is 5 mm. b) Representative fluorescence microscopy images of primary hippocampal neuron cultures incubated with (top image) or without (bottom image) SOs stained with phalloidin-FITC to visualize neurite and axonal connectivity.

After release from the stabilizing w/o droplet shell, the magnetosome-like SOs were readily taken up by normal rat kidney fibroblasts. Transmission electron microscopy (TEM) analysis of the cells and the internalized SOs confirmed that the iron nanoparticles remained in their GUV shell after uptake (Figure S3a, Supporting Information). Importantly, when analysing the actin cytoskeleton configuration around the synthetic magnetosomes using phalloidin-FITC staining, we found coupling of the SOs to the actin network. This suggests that mechanical forces applied from inside the SOs using magnetic field deflecting Fe-NPs could be transmitted to the surrounding actin cytoskeleton (Figure S3b, Supporting Information).

In order to assess to which extent synthetic magnetosome-loaded cells can sense, align, and even migrate within a magnetic field, we incubated SO-loaded fibroblast cell layers next to a commercially available AlNiCo permanent magnet (see the Experimental Section). Bright field microscopy performed 24 h after loading showed that the synthetic magnetsomes align within the cytoplasm of the cells and can even form pearl-like strings reminiscent of bacterial magnetosome architectures (Figure 4c). These results indicate that the iron nanoparticles are deflected by the magnetic field even within the intracellular environment, resulting in the alignment of the magnetic particles along the field.

In order to analyse if the migratory behaviour of the fibroblasts is affected by the magnetic field and the intracellular alignment of the NPs, we stained SOs-loaded cells with phalloidin-FITC and Hoechst 33 342, 48 h after incubation within 24-well plates next to an AlNiCo magnet. By imaging the complete wells, we analysed actin distribution to assess cell distribution within the wells. In wells incubated alongside a magnet, we found extensive cell aggregation on the side closer to the magnet, whereas cell layers cultured without a magnet showed

homogeneous cell distribution within the wells (Figure 4d). Automated counting of cell nuclei revealed that cell density next to the magnet was approximately three times higher than on the opposite side of the well, which confirmed our observations on stained actin distribution. This demonstrates that cells equipped with a synthetic magnetosome gained the ability to sense and migrate with a magnetic field.

As fibroblasts are intrinsically highly motile cells,[22] we aimed to assess whether this concept could also be expanded to other less motile cell types. In this regard, the controlled migration of neuronal cells is of especially great interest due to its relevance for the treatment of spinal cord injuries like cross section paralysis or other types of neuronal palsy and damage.[23] We therefore introduced synthetic magnetosomes into primary rat hippocampal neurons and incubated them alongside an AlNiCo paramagnet for 96 h. We subsequently analysed phalloidin-FITC and Hoechst 33342-stained cultures for cell density distribution. We found that cell density next to the magnet was approximately twice as high as compared to cells not cultured next to a magnet (**Figure 5**a). Importantly, these cells also displayed increased connectivity and actin enrichment, presumably because of the increased mechanical forces within the network, a known stimulant of neurite and axonal growth (Figure 5b).[24,25]

3. Conclusion and Outlook

Taking advantage of the unique capabilities of microfluidic-based GUV assembly, we successfully produced functional SOs and demonstrated their uptake into different mammalian cell types, including primary cells. We show that GUV-based SOs can be equipped with diverse operational modules that mimic

**ADVANCED
SCIENCE NEWS**
www.advancedsciencenews.com

NANO · MICRO
small
www.small-journal.com

natural organelle structure and function inside of living cells. Employing microfluidics for the production of lipid enveloped SOs is a fundamental advancement, as this technology is compatible with numerous classes of lipids that allow to precisely recapitulate the natural organelle membrane composition. It takes the incorporation of compounds into the SO lumen to a new level, as it functions with a variety of sizes ranging from low molecular weight compounds like npEGTA cages to large particles like iron nanoparticles. This opens the door for the construction of complex, higher order machineries operable in the intracellular space. Moreover, the microfluidic GUV production technology also allows for the production of multicompartment vesicles.[11] Therefore, SOs with even more complex functionalities like sequential release of compounds or further multistep biochemical reactions could be assembled.

By copying the core enzymatic apparatus of peroxisomes, we show that SO-entrapped enzymes are functional after uptake into the intracellular space and that SOs can support fundamental cellular metabolic processes like redox equilibration. Moreover, we demonstrate that SOs provide a means for introducing artificial regulatory elements which respond to external stimuli into cells. This allows external alteration and interference with key cellular functionalities like intercellular signalling. Autonomous SOs that can be dynamically triggered (e.g., by light stimulation), could in future advance investigations on the origin and function of natural organelles. Importantly, our microfluidic approach is not restricted to the production of SOs that simply recreate the functionality of natural organelles. Instead, it allows for expanding the borders of natural design and building plans toward new synthetic modules. By rebuilding a synthetic magnetosome that provides a magnetotactic sense to mammalian cells, we provide a proof-of-concept for how SOs could in future serve as versatile tools to expand the natural repertoire of cellular functions. Moreover, as novel therapeutic compounds, SOs could replace, rescue, or support deregulated or dysfunctional organelles in disease states.

In a next step, more options are needed to control the intracellular stability of implanted SOs. Thus far, we have observed stable intracellular SOs for as long as 72 h. This constitutes a time window that is well suited for the in vitro analysis of organelle function and medical approaches aiming for transient intervention but it is less applicable for procedures involving long-lasting effects. In particular, the ability to escape lysosomal degradation could significantly extend SO stability. In far future, SOs might even be equipped with modules that allow their replication during the cell cycle, allowing for a true fusion with the living cell.

Importantly, the foundation of our approach, the high-throughput microfluidic production pipeline, allows us to "transfect" millions of cells with SOs in vitro. This paves the way toward the equipment of cell cultures used in industrial production plants with SOs. The introduction of, for example, peroxisome mimics to support cellular stress management could increase the yield of bioproduct of interest. Moreover, SOs that harbor natural or synthetic molecular machineries capable of catalyzing specific biological reactions could be implanted into living cells. "Feeding" from natural cellular educts, such artificial organelles could serve as intracellular production plants not only for isolating toxic intermediates and side products from the cytoplasm but also for increasing the yields and purity of biotechnological products.

4. Experimental Section

Materials: EggPG, EggPC, 18:1 LissRhodamine B PE, and an extrude set with 50 nm pore size polycarbonate filter membranes were purchased from Avanti Polar Lipids, USA. All lipids were stored in chloroform at −20 °C and used without further purification. PFPE-PEG block-copolymer fluorosurfactant was purchased from Ran Biotechnologies, USA. Bovine catalase, Menadione, <50 nm Fe_2O_3 nanoparticles propidium iodide, and Phalloidin-FITC were obtained from Sigma Aldrich (Germany). CellRox Green reagent, CellTracker Green CMFDA dye, Hoechst 33 342, Fluo-4 AM-ester, *o*-nitrophenyl EGTA tetrapotassium, wheat germ agglutinin Alexa Fluor 647 conjugate, heat inactivated fetal bovine serum, penicillin-streptomycin (10 000 U mL^{-1}), L-Glutamine (200 × 10^{-3} M), trypsin-EDTA (0.05%) with phenol red, and phosphate buffered saline were purchased from Thermo Fischer Scientific (Germany). HaCaT keratinocytes were obtained from C-Line Products (Germany). Normal rat kidney cells and BJ fibroblasts were purchased from ATCC (USA). Primary hippocampal neurons were a generous gift from Dr. Elisa D'Este (Max Planck Institute for Medical Research). Cultures of hippocampal neurons were prepared from Wistar rats of mixed sex at postnatal day P0–P1 in accordance with the Animal Welfare Law of the Federal Republic of Germany (Tierschutzgesetz der Bundesrepublik Deutschland, TierSchG) and the Regulation about animals used in experiments (1st August 2013, Tierschutzversuchsverordnung). For the procedure of sacrificing rodents for subsequent preparation of any tissue, all regulations given in §4 TierSchG were followed. Since sacrificing of animals is not an experiment on animals according to §7 Abs. 2 Satz 3 TierSchG, no specific authorization or notification is required.

Cell Culture: HaCaT, normal rat kidney cells- and BJ fibroblasts were culture in Dulbecco's Modified Eagle Medium supplemented with 10% fetal bovine serum, 1% penicillin/streptomycin, and 1% L-glutamine at 37 °C and in a humidified 5% CO_2 atmosphere. Cell cultures were routinely subcultured by trypsinization at ≈80% confluency.

Microfluidic-Based GUV Production: dsGUVs were produced from SUV solution composed of 20 mol% EggPG, 79% EggPC, and 1 mol% 18:1 LissRhodamine B PE. In brief, lipids dissolved in chloroform were mixed at desired ratios in glass vials and dried under a gentle nitrogen stream. The dried lipid film was rehydrated to a final lipid concentration of 3 × 10^{-3} M in PBS containing 10 × 10^{-3} M $MgCl_2$. The solution was shaken for 5 min at min. 600 rpm. This liposome solution was extruded at least nine times through a 50 nm pore size polycarbonate filter. The SUV solution was either stored at 4 °C for up to 3 days or used for dsGUV production immediately.

Droplet-based microfluidic devices were fabricated from PDMS. The devices were produced as described in previous communications using photo- and soft-lithography methods.[4] Water and oil flow rates were controlled by an Elveflow OB1 MK3-microfluidic flow control system. For the formation of dsGUVs within microfluidic droplets, the SUV solutions were diluted to a final lipid concentration of 1.5 × 10^{-3} M. The SUV solution was introduced into the aqueous channel of the microfluidic devices for droplet formation. GUVs were formed using 1.25 × 10^{-3} M PFPE$_{(7000\ g\ mol^{-1})}$-PEG$_{(1500\ g\ mol^{-1})}$-PFPE$_{(7000\ g\ mol^{-1})}$ triblock surfactant dissolved in FC-40 oil. A water to oil phase ratio of ≈1:4 was used for all droplet productions. Droplets with a size of ≈10 µm diameter were formed at the flow-focusing junction and collected from the outlet of the microfluidic chip into a microcentrifuge tube. Subsequently, dsGUVs were allowed to equilibrate for a minimum of 2 h at 4 °C before performing the release procedure.

For the release of dsGUVs from the stabilizing polymer shell, the excess oil phase was removed from the microtube by pipetting. The residual droplet layer was mixed at a volume ratio of 1:1:1 (aq. production buffer : PBS : destabilizing PFO) with low molecular weight PFO destabilizing surfactant. Following 30 min of equilibration, the GUV-containing upper aqueous layer was transferred into a 2 mL microtube. PBS was added to a total volume of 2 mL and GUVs were

centrifuged at >10 000 g for 15 min to remove residual SUVs or rupture GUV components. The supernatant was removed and the GUV pellet was resuspended in 200 µL PBS.

For production of catalase containing GUVs, bovine catalase was added at a final concentration of 2.7×10^{-3} M to the SUV solution used for dsGUV production. For production of np-EGTA containing GUVs, we mixed np-EGTA and $CaCl_2$ at an equimolar ratio to a final concentration of 10×10^{-3} M and added to the SUVs used for droplet production. During the production of np-EGTA containing GUVs all steps were carried out in the dark or if not possible under red light. For production of dsGUVs that contain Fe_2O_3 nanoparticles, the nanoparticles were dissolved to a final concentration of 100 µg mL^{-1} in 0.1% w/v bovine serum albumin. This solution, which also contained the SUVs, was used for dsGUV production.

Analysis of SOs Uptake: To analyze SOs uptake, respective SOs were incubated with HaCaT keratinocytes for 24 h at 37 °C and 5% CO_2 in serum supplemented cell culture medium. Directly after addition of the SOs to the cells, 5 µg mL^{-1} Alexa Fluor647 conjugated wheat germ agglutinin (WGA) was added to stain cell membranes and as a consequence of membrane turnover also endosomes. After incubation, cells were washed twice with PBS to remove excess GUVs and stained with 2 µg mL^{-1} Hoechst33342 and CellTracker Green CMFDA dye following the manufacturer's instructions. Confocal microscopy was used to identify endocytosed GUVs as follows: they exhibited Rhodamine B fluorescence, were surrounded by a WGA Alexa Fluor647-stained endosomal membrane, and did not show any cytoplasmic staining.

Dead Cell Quantification: SOs induced cytotoxicity was analyzed by quantification of propidium iodide (PI) staining intensity in plate reader measurements. NRK cells were seeded in 96 flat-bottom transparent well-plates for 24 h in growth medium and allowed to form confluent monolayers. Subsequently, respective GUVs were added to the cells and incubated for 72 h. For control measurements, cells were either left untreated or incubated with 10% w/v Tween-20. PI was added to a final concentration of 1 µg mL^{-1} and incubated for 30 min before analysis. PI fluorescence in each well was measured at four different positions using an Infinite M200 TECAN plate reader controlled by TECAN iControl software with an in-built gain optimization and excitation/emission setting adjusted to 535/617 nm. Three technical replicates were performed for each condition.

Oxidative Stress Induction and ROS Quantification: For the induction of oxidative stress in HaCaT cultures, cells were seeded in a 96-well plate format and incubated to form a confluent monolayer (≈50 000 cells per well) after 24 h. After monolayer formation, SOs were added to the cells and incubated for 24 h to allow internalization. Subsequently, noninternalized SOs were washed away by 2× PBS washing. Next, menadione was added to a final concentration of 25×10^{-3} M and the plates incubated for 1 h. CRG was then added to the cells following the manufacturer's instructions. CRG staining was quantified using an Infinite M200 TECAN plate reader controlled by TECAN iControl software with an in-built gain optimization and excitation/emission setting adjusted to 488/525 nm or imaged by epifluorescence microscopy.

Assessment of SOs Containing npEGTA-Caged Ca^{2+}: For the implantation of npEGTA-caged Ca^{2+} harboring SOs, BJ dermal fibroblast were cultured to form a confluent monolayer 24 h after seeding. Subsequently, SOs were added to the cells and incubated overnight to allow internalization. All procedures were carried out in the dark or under red light illumination. Before microscopy analysis, cells were stained with cell permeable fluo-4 AM ester following the manufacturer's recommendations. For UV-mediated Ca^{2+} uncaging, cells were washed twice with PBS to remove non-uptaken GUVs and then imaged by confocal microscopy. A region of interest containing uptaken SOs was illuminated at full laser power for five iterations and the fluo-4 signal recorded over time. For the analysis of spontaneous pacemaker activity in fibroblast monolayers, BJ monolayers were stained with fluo-4 AM ester and imaged by time-lapse confocal microscopy.

For entrapping npEGTA-Ca^{2+}-containing GUVs within water-in-oil droplets, a $MgCl_2$-free PBS solution containing GUVs was used as the aqueous phase for droplet production. A final concentration of 200×10^{-3} M fluo-4 was added to this solution. To avoid fusion of the GUVs at the droplet periphery, a FC40 solution containing 1% w/v commercially available PFPE carboxylic acid free surfactant (RAN biotechnologies surfactant) was used. Water-in-oil droplets were produced following a manual shaking protocol published previously and droplets were imaged and uncaged following the procedure detailed above for cell lines.[11]

Time-resolved mean signaling intensity profiles from cells and droplets were monitored by manual selection of areas of interest using ImageJ software.

Analysis of Magnetotactic Behavior of SO-Loaded Fibroblasts and Hippocampal Neurons: For analyzing the magnetic field-induced deflection of Fe_2O_3 nanoparticle-containing dsGUVs, time-lapse confocal microscopy was employed. An AlNiCo magnet was manually placed next to the sample during acquisition, avoiding any mechanical shaking of the setup to avoid vibration-induced deflections.

To analyze the intracellular integration of magnetosome-like SOs after uptake, normal rat kidney cells were seeded in 24 well plates at a density of 300 000 cells per well. After overnight incubation, SOs were added to the cells and incubated for 24 h to allow internalization. Subsequently, cell layers were washed twice with PBS to remove non-uptaken SOs and an AlNiCo magnet was placed next to the cultures (or cells were cultured without a magnet as control). Cells were cultured in this configuration for 48 h and subsequently fixed with 4% *para*-formaldehyde for 20 min. Before imaging by bright field and epifluorescence microscopy, cells were stained with 2 µg mL^{-1} Hoechst 33 342 and phalloidin-TRITC for 1 h. The same procedure was applied to primary hippocampal neurons with the exception that the incubation time was prolonged to 96 h. Actin configuration around internalized magnetosome-like SOs was assessed by imaging phalloidin-TRITC stained rat embryonic fibroblast cultures.

Global histogram-based intensity thresholding segmentation was applied to the nuclear stain images for an automated local cell density analysis. Images were separated manually into the corresponding regions and particles were counted with the built-in particle counter from ImageJ software.

Microscopy: For fluorescence confocal microscopy analysis, cell lines were cultured in 8-well Nunc LabTeK glass bottom culture slides filled with a minimum of 400 µL fully supplemented culture medium. Confocal microscopy was performed using a laser scanning microscope LSM 800 (Carl Zeiss AG). Images were acquired using a 20× (Objective Plan-Apochromat 20×/0.8 M27, Carl Zeiss AG) and a 63× immersion oil objective (Plan-Apochromat 63×/1.40 Oil DIC, Carl Zeiss AG). Images were analyzed using ImageJ (NIH) software. For time-lapse live cell imaging by bright field and epifluorescence microscopy, a Leica DMi8 inverted fluorescent microscope equipped with a sCMOS camera and 10× HC PL Fluotar (NA 0.32, PH1) objective as well as a temperature and CO_2 chamber was used. Adjustments of image brightness and contrast as well as background corrections were always performed on the whole image and care was taken not to obscure or eliminate any information from the original image (this also applies for TEM images).

TEM: Normal rat kidney cells incubated for 24 h with magnetosome-like SOs were fixed in 2.5% glutaraldehyde dissolved in a 0.1 M Na_3PO_4 solution for 60 min at room temperature. Cells were further fixed using 0.4% uranyl acetate overnight. Dehydration of the fixed cells was performed by a 50%, 60%, 70%, 80%, 90%, and 100% ethanol series and embedded in resin over night at 60 °C. 85 nm ultrathin sections were cut and contrasted with lead acetate or osmium tetroxide. For imaging, a Zeiss EM 10 CR TEM was used. Whenever necessary, image contrast, brightness and sharpness were adjusted using the built-in ImageJ plug-ins.

Supporting Information

Supporting Information is available from the Wiley Online Library or from the author.

[1] K. Gopfrich, I. Platzman, J. P. Spatz, *Trends Biotechnol.* **2018**, *36*, 938.

[2] M. P. N. Juniper, M. Weiss, I. Platzman, J. P. Spatz, T. Surrey, *Soft Matter* **2018**, *14*, 901.

[3] S. Wang, S. Majumder, N. J. Emery, A. P. Liu, *Synth. Biol. (Oxford, England)* **2018**, *3*, ysy005.

[4] M. Weiss, J. P. Frohnmayer, L. T. Benk, B. Haller, J. W. Janiesch, T. Heitkamp, M. Borsch, R. B. Lira, R. Dimova, R. Lipowsky, E. Bodenschatz, J. C. Baret, T. Vidakovic-Koch, K. Sundmacher, I. Platzman, J. P. Spatz, *Nat. Mater.* **2018**, *17*, 89.

[5] S. M. Bartelt, J. Steinkuhler, R. Dimova, S. V. Wegner, *Nano Lett.* **2018**, *18*, 7268.

[6] L. M. P. E. van Oppen, L. K. E. A Abdelmohsen, S. E. van Emst-de Vries, P. L. W. Welzen, D. A. Wilson, J. A. M. Smeitink, W. J. H. Koopman, R. Brock, P. H. G. M. Willems, D. S. Williams, J. C. M. van Hest, *ACS Cent. Sci.* **2018**, *4*, 917.

[7] T. Einfalt, D. Witzigmann, C. Edlinger, S. Sieber, R. Goers, A. Najer, M. Spulber, O. Onaca-Fischer, J. Huwyler, C. G. Palivan, *Nat. Commun.* **2018**, *9*, 1127.

[8] K. Y. Lee, S. J. Park, K. A. Lee, S. H. Kim, H. Kim, Y. Meroz, L. Mahadevan, K. H. Jung, T. K. Ahn, K. K. Parker, K. Shin, *Nat. Biotechnol.* **2018**, *36*, 530.

[9] C. D. Reinkemeier, G. E. Girona, E. A. Lemke, *Science* **2019**, *363*, eaaw2644.

[10] B. Haller, K. Gopfrich, M. Schroter, J. W. Janiesch, I. Platzman, J. P. Spatz, *Lab Chip* **2018**, *18*, 2665.

[11] K. Göpfrich, B. Haller, O. Staufer, Y. Dreher, U. Mersdorf, I. Platzman, J. P. Spatz, *ACS Synth. Biol.* **2019**, *8*, 937.

[12] J. W. Janiesch, M. Weiss, G. Kannenberg, J. Hannabuss, T. Surrey, I. Platzman, J. P. Spatz, *Anal. Chem.* **2015**, *87*, 2063.

[13] R. M. Straubinger, K. Hong, D. S. Friend, D. Papahadjopoulos, *Cell* **1983**, *32*, 1069.

[14] G. van Meer, A. I. de Kroon, *J. Cell Sci.* **2011**, *124*, 5.

[15] J. Kruk, E. Duchnik, *Asian Pac. J. Cancer Prev.* **2014**, *15*, 561.

[16] G. Loor, J. Kondapalli, J. M. Schriewer, N. S. Chandel, T. L. Vanden Hoek, P. T. Schumacker, *Free Radical Biol. Med.* **2010**, *49*, 1925.

[17] C. Vasquez, N. Benamer, G. E. Morley, *J. Cardiovasc. Pharmacol.* **2011**, *57*, 380.

[18] A. Sebastian, F. Syed, D. A. McGrouther, J. Colthurst, R. Paus, A. Bayat, *Exp. Dermatol.* **2011**, *20*, 64.

[19] O. Staufer, S. Weber, P. Begntson, H. Bading, A. Rustom, J. P. Spatz, *Nano Letters* **2019**, *19*, 3244.

[20] W. J. Parak, J. Domke, M. George, A. Kardinal, M. Radmacher, H. E. Gaub, A. D. de Roos, A. P. Theuvenet, G. Wiegand, E. Sackmann, J. C. Behrends, *Biophys. J.* **1999**, *76*, 1659.

[21] M. Blondeau, Y. Guyodo, F. Guyot, C. Gatel, N. Menguy, I. Chebbi, B. Haye, M. Durand-Dubief, E. Alphandery, R. Brayner, T. Coradin, *Sci. Rep.* **2018**, *8*, 7699.

[22] R. J. Petrie, K. M. Yamada, *Trends Cell Biol.* **2015**, *25*, 666.

[23] S. Shibuya, T. Yamamoto, T. Itano, *Cell Adhes. Migr.* **2009**, *3*, 99.

[24] V. Raffa, F. Falcone, S. De Vincentiis, A. Falconieri, M. P. Calatayud, G. F. Goya, A. Cuschieri, *Biophys. J.* **2018**, *115*, 2026.

[25] J. Zheng, P. Lamoureux, V. Santiago, T. Dennerll, R. E. Buxbaum, S. R. Heidemann, *J. Neurosci.* **1991**, *11*, 1117.